Spectrum and low-energy gap in triangular quantum spin liquid NaYbSe$_2$

A. O. Scheie,[1, *] Minseong Lee,[2, †] Kevin Wang,[3] P. Laurell,[4] E. S. Choi,[5] D. Pajerowski,[6] Qingming Zhang,[7] Jie Ma,[8] H. D. Zhou,[4] Sangyun Lee,[2] S. M. Thomas,[1] M. O. Ajeesh,[1] P. F. S. Rosa,[1] Ao Chen,[9] Vivien S. Zapf,[2] M. Heyl,[9] C. D. Batista,[4, 6] E. Dagotto,[4, 10] J. E. Moore,[3, ‡] and D. Alan Tennant[4, 11, §]

[1]*Los Alamos National Laboratory, Los Alamos, NM 87545, USA*
[2]*National High Magnetic Field Laboratory, Los Alamos National Laboratory, Los Alamos, New Mexico 87545, USA*
[3]*Department of Physics, University of California, Berkeley, CA 94720, USA*
[4]*Department of Physics and Astronomy, University of Tennessee, Knoxville, TN 37996, USA*
[5]*National High Magnetic Field Laboratory, Florida State University, Tallahassee, FL 32310, USA*
[6]*Neutron Scattering Division, Oak Ridge National Laboratory, Oak Ridge, TN 37831, USA*
[7]*School of Physical Science and Technology, Lanzhou University,*
Institute of Physics, Chinese Academy of Sciences, Lanzhou 730000, China
[8]*Department of Physics and Astronomy, Shanghai Jiao Tong University, Shanghai 200240, China*
[9]*Theoretical Physics III, Center for Electronic Correlations and Magnetism,*
Institute of Physics, University of Augsburg, D-86135 Augsburg, Germany
[10]*Materials Science and Technology Division, Oak Ridge National Laboratory, Oak Ridge, TN 37831, USA*
[11]*Department of Materials Science and Engineering, University of Tennessee, Knoxville, TN 37996, USA*
(Dated: June 26, 2024)

We report neutron scattering, pressure-dependent AC calorimetry, and AC magnetic susceptibility measurements of triangular lattice NaYbSe$_2$. We observe a continuum of scattering, which is reproduced by matrix product simulations, and no phase transition is detected in any bulk measurements. Comparison to heat capacity simulations suggest the material is within the Heisenberg spin liquid phase. AC Susceptibility shows a significant 23 mK downturn, indicating a gap in the magnetic spectrum. The combination of a gap with no detectable magnetic order, comparison to theoretical models, and comparison to other AYbSe$_2$ compounds all strongly indicate NaYbSe$_2$ is within the quantum spin liquid phase. The gap also allows us to rule out a gapless Dirac spin liquid, with a gapped $\mathbb{Z}_2$ liquid the most natural explanation.

A quantum spin liquid (QSL) is a state of matter first predicted by P. W. Anderson in 1973, wherein spins arranged in a lattice exhibit a massively entangled and fluctuating ground state [1]. One defining characteristic of QSLs is their fractional excitations, which interact with each other through emergent gauge fields [2, 3]. The potential for topological protection from decoherence makes QSLs appealing platforms for quantum technologies. However, despite decades of searching and extensive theoretical work, no unambiguous examples of a quantum spin liquid material have been found.

Anderson's original prediction for a QSL state was the two-dimensional triangular lattice antiferromagnet. With nearest-neighbor exchange only, this system orders magnetically, but a small antiferromagnetic second-nearest-neighbor exchange J_2 theoretically stabilizes a QSL phase [4–10]. Though the existence of this phase is well-accepted theoretically (although not experimentally until now), it is not clear what kind of QSL such a state would be. Proposals include a gapless $\mathbb{U}_1$ Dirac QSL [6, 10–12], a valence bond crystal [13, 14], a gapped $\mathbb{Z}_2$ QSL [4, 5, 15, 16], or a chiral spin liquid [17]. Because numerical simulations are limited by finite size, theoretical results are ambiguous [13, 18]. The best (and perhaps only) way to resolve this question would be to find a real material which harbors the triangular lattice QSL ground state.

Inelastic neutron scattering studies of triangular antiferromagnets with nearest-neighbor exchange have revealed anomalous continuum scattering that cannot be explained by semiclassical theories [19–21]. The measured single-magnon dispersion was accurately reproduced using a Schwinger Boson approach, where magnons are obtained as two-spinon bound states [22, 23]. This suggests that these ordered magnets are in close proximity to a gapped $\mathbb{Z}_2$ QSL as the deconfined Schwinger Boson phase. But an unambiguous measurement of a material in the deconfined QSL phase has not been reported.

A very promising class of materials is the Yb delafossites AYbSe$_2$ where A is an alkali metal [24–29]. These form ideal triangular lattices of magnetic Yb^{3+}, and appear to approximate the Heisenberg J_2/J_1 model [30], see Fig. 1. Of these, CsYbSe$_2$ and KYbSe$_2$ have been observed to order magnetically at zero field [28, 29]. However, following a trend in the periodic table that a smaller A-site element enhances J_2 and destabilizes order [30], no long-range magnetic order has been observed in NaYbSe$_2$ [24, 27], which makes it a prime candidate for a QSL ground state. Importantly, the tunability of these compounds means that the QSL phase can be approached systematically from magnetic order (Fig. 1). This allows for greater confidence and rigor than studying a single compound in isolation would.

Previous NaYbSe$_2$ studies reported a diffuse neutron spectrum that was interpreted in terms of spinon Fermi surface excitations from a QSL [27], but because of 3% Na site disorder on those samples, it is not clear whether the magnetic order and coherent excitations were destroyed by small amounts of

* scheie@lanl.gov
† ml10k@lanl.gov
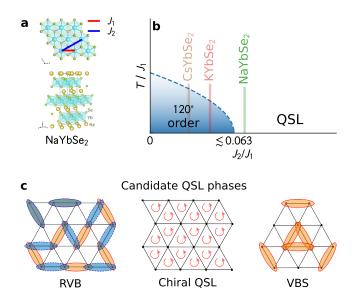‡ jemoore@berkeley.edu
§ dtennant@utk.edu

FIG. 1. Triangular lattice quantum spin liquid (QSL). Panel **a** shows the NaYbSe$_2$ crystal structure. Panel **b** shows the conceptual phase diagram of CsYbSe$_2$, KYbSe$_2$, and NaYbSe$_2$ as a function of fitted J_2/J_1 values [30]. The theoretical boundary to the quantum spin liquid phase for the isotropic model is detected by neural quantum state (NQS) simulations at $J_2/J_1 \lesssim 0.063 \pm 0.001$ (see Supplemental Materials) locating NaYbSe$_2$ well within the QSL phase. Panel **c** shows schematics for potential gapped phases on the triangular lattice: the gapped $\mathbb{Z}_2$ QSL as resonating valence bond (left), a chiral QSL (center), and a particular ordering pattern [14] for a 12-site valence bond solid (right). Note: overlapping ovals represent resonating singlet bonds.

disorder (as in the ill-fated Yb^{3+} QSL candidates YbMgGaO$_4$ [31] and Yb$_2$Ti$_2$O$_7$ [32]). To further clarify NaYbSe$_2$, we measured the inelastic neutron spectra, AC calorimetry, and AC susceptibility with high quality samples. We observe coherent excitations, lack of magnetic order, and evidence in bulk susceptibility of a 2.1 μeV gap at low temperature. This is strong evidence for a QSL ground state in NaYbSe$_2$ and a gapped QSL on the triangular lattice.

The neutron spectra at 100 mK, shown in Fig. 5, show a highly dispersive continuum of excitations with a well-defined lower bound, similar to KYbSe$_2$ [28] (see supplemental materials for experimental details). This is qualitatively different from the spectra measured by Dai et al [27] on the 3% Yb/Na site-mixed sample which in contrast showed smeared our continua in k-space and diffuse spectra extending to low energies in many regions of reciprocal space. (Later in the text, we will explain why we believe our samples are free from mixing disorder.) Here, the only region of reciprocal space which has appreciable intensity down to low energies is $(1/3, 1/3, 0)$, corresponding to the 120° magnetic order seen in sister compounds KYbSe$_2$ [28] and CsYbSe$_2$ [29]. Down to 50 μeV (the limit before the incoherent scattering on the elastic line obscures the scattering energy for the incident energy of $E_i = 1$ meV), no gap in the spectrum is resolved.

For comparison we also show matrix product state (MPS) calculated spectra in 5**f-i** with $J_2/J_1 = 0.071$ (this value de-

rived from finite field non-linear spin wave fits [30]), at varying levels of exchange anisotropy Δ (see Supplemental Materials). The boundary to the quantum spin liquid phase for the isotropic model is at $J_2/J_1 = 0.063$ calculated using neural quantum states (see Supplemental Materials) locating the material in the theoretically predicted QSL phase for weak anisotropies. Because of finite size lattice effects the calculated spectra are gapped, and it is difficult to make quantitative comparisons between theory and neutron experiments. Nevertheless, the calculated spectra are consistent with the observed spectra, corroborating the idea that a J_2/J_1 model with easy-plane anisotropy is an appropriate model for NaYbSe$_2$.

Despite intensity concentrated at $(1/3, 1/3, 0)$ and similar spectra to CsYbSe$_2$ and KYbSe$_2$, we observe no static magnetic order in NaYbSe$_2$ in neutron scattering measurements down to 100 mK. No magnetic ordering features are visible in heat capacity down to 100 mK either, as shown in Fig. 3. (Note also that our sample has similar low-temperature specific heat to those reported in Refs. [25, 33]. If the C/T maximum at 800 mK is an indication of sample quality, our sample is free from the site mixing reported in Ref. [27].) To test whether applied hydrostatic pressure can induce order—as in KYbSe$_2$ wherein pressure enhanced T_N [30]—we also measured AC calorimetry under pressure (see Supplemental Materials) shown in Fig. 3**b**. Up to 2.0 GPa, no sharp feature as expected for an ordering transition is seen in the data (pressure-dependent thermalization issues cause the low-T specific heat to increase at low T, but this is a known artifact and would not mask a sharp ordering transition).

Also in Fig. 3**c** we compare NaYbSe$_2$ heat capacity to KYbSe$_2$, with the temperature axis rescaled by the fitted J_1 [30]. This shows not only a lack of ordering transition, but also a smaller $k_B T/J_1 \approx 0.2$ maximum heat capacity and greater low-temperature heat capacity in NaYbSe$_2$ relative to KYbSe$_2$. Comparing this to thermal pure quantum state (TPQ) simulations of the 27-site 2D triangular lattice in Fig. 3**d**, these trends are beautifully explained with a larger J_2/J_1 in NaYbSe$_2$: the low-temperature heat capacity is largest when $J_2/J_1 \approx 0.07$ and the $k_B T/J_1 = 0.2$ bump is suppressed with larger J_2. Because the TPQ simulations are of a finite size cluster which induces an artificial energy gap, the lowest temperature trends are not quantitatively accurate. However, on a qualitative level, this is remarkable confirmation that NaYbSe$_2$ is indeed closer to or inside the triangular QSL phase.

To investigate the magnetic state to lower temperatures, we measured AC susceptibility down to 20 mK with AC and DC field applied along the a and c directions on NaYbSe$_2$ (see Supplemental Materials). In this case we observe a clear magnetization plateau in the $B \parallel a$ direction at 5 T, but not for $B \parallel c$ (note these data were collected simultaneously on two separate crystals mounted on two separate susceptometers mounted on the same dilution refrigerator). This agrees with previous measurements [25], and indicates an easy-plane exchange anisotropy in NaYbSe$_2$: in the perfectly isotropic triangular model, 1/3 magnetization plateaux appear both in-plane and out-of-plane, but the out-of-plane plateau is suppressed by planar anisotropy [34–36], although the in-plane
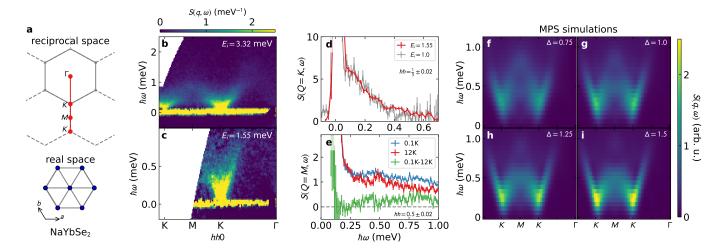
FIG. 2. Neutron scattering data on NaYbSe$_2$. Panel **a** shows the triangular crystal structure and reciprocal space vectors, with hh vertical. Panels **b** and **c** show neutron scattering in the $hh\ell$ scattering plane, integrated over $\ell < 4.5$ reciprocal lattice units (rlu) with incident neutron energies $E_i = 3.32$ meV and 1.55 meV respectively. 12 K data have been subtracted as a background, see supplemental materials. Panel **d** shows the scattering at K= (1/3, 1/3, 0) as a function of energy with $E_i = 1.0$ meV and 1.55 meV. To an energy resolution of 50 μeV, the spectrum is gapless. Panel **e** shows the temperature-subtracted scattering at M= (1/2, 1/2, 0) with $E_i = 3.32$ meV, and it is unclear whether the spectrum is gapped or gapless at M. Panels **f**-**i** show MPS simulated scattering of NaYbSe$_2$ with varying levels of anisotropy. Note the broadened signal due to finite size effects.
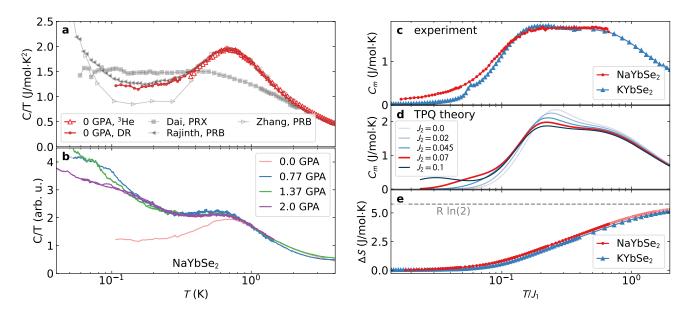

FIG. 3. NaYbSe$_2$ specific heat. Panel **a** shows ambient pressure specific heat, measured with both a ^{3}He PPMS insert and the dilution refrigerator (DR). In grey are the data from previous studies [25, 27, 33]. Panel **b** shows pressure dependent heat capacity. The low-temperature upturn is an artifact of measuring in a pressure medium with finite thermal conductivity, but no pressure-induced magnetic ordering transition is visible in the data. Panel **c** shows the magnetic specific heat of NaYbSe$_2$ compared to KYbSe$_2$ [28], with the temperature axis scaled by $k_B J_1$ for each compound. Panel **d** shows the theoretical calculated specific heat from TPQ (see text) as a function of J_2 in units of J_1. The theoretical trend confirms that NaYbSe$_2$ is closer to the QSL. Panel **e** shows the integrated entropy, revealing that both compounds converge close to $R\ln(2)$.

magnetism still has a continuous rotation symmetry and similar physics is preserved.

However, the most important feature in susceptibility is the low-field drop in susceptibility at 23 mK, shown in Fig 4**b** and **e**. This drop occurs in both the $B \parallel a$ and $B \parallel c$ data. Observing such a feature at such low temperatures is *prima facie* evidence of high crystalline quality: any magnetic randomness or disorder in the material must involve an energy smaller than $\sim k_B T = 2.2\,\mu$eV, or else such a feature would be suppressed. Furthermore, there is no detectable frequency dependence in either direction, shown in Fig. 4**c** and **f**, indicating that it is not a spin-freezing transition. Rather, this indicates

either a magnetic ordering transition, or a gap opening in the magnetic excitations.

If the 23 mK susceptibility feature were a magnetic ordering transition, this would indicate that NaYbSe$_2$ is extremely close to a QSL phase, closer than any other triangular delafossite materials [30]. The order would be extremely subtle, as the temperature $\frac{23\,\mathrm{mK}}{J_1/k_B} \approx 1/280$ means the amount of energy available for *any* type of order is very small, i.e., the order parameter saturates to a tiny value, and the system is left mostly fluctuating. However, the hypothesis of 23 mK magnetic order is unlikely, for three reasons.

First, the isotropy: the drop in susceptibility is qualitatively the same along a and c. The only difference at zero field is a slightly higher peak temperature for $H \parallel c$ at 24 mK. Antiferromagnetic order (especially the coplanar order expected for NaYbSe$_2$ with planar anisotropy) should produce a very different response for the field along which the spins order. Meanwhile, a gapped spectrum produces an isotropic response, consistent with what is observed here.

Second, the magnitude: the drop in susceptibility is more than 5% without background susceptibility subtracted, whereas an ordering transition at such extremely low temperatures (in comparison to a ~ 15 K bandwidth) would indicate very weak order with an extremely small recovered entropy, and a correspondingly weak signal in bulk properties. Indeed, in the sister compound KYbSe$_2$, despite a clear magnetic order transition at 290 mK in heat capacity and neutron diffraction [28], the ordering feature in susceptibility is essentially invisible (see Supplemental Fig. 11). If the NaYbSe$_2$ shows the same antiferromagnetic ordering and the ordering temperature is an order of magnitude lower in temperature than KYbSe$_2$, we would expect a much weaker feature in susceptibility. Instead we observe a very strong feature, which is evidence for it being from a gapped spectrum. This abrupt drop is also inconsistent with spin glass behavior, where the ac susceptibility typically shows a frequency-dependent peak and symmetric decrease both above and below the peak temperature.

Third, fine-tuning: such a low transition temperature would require the system to sit exactly on the boundary between the QSL and AFM order. If we assume the system lies within the 120° ordered phase, the dynamical exponent of the critical point would be $z = 1$ (linearly dispersing zero modes). This implies that the effective dimension of the theory that describes the quantum phase transition is $D = d + z = 3 + 1 = 4$. Since $D = 4$ is the upper critical dimension (Gaussian fixed point), we expect the behavior of $T_N(J_2/J_1)$ to be mean field like, i.e., $T_N \propto \sqrt{J_2^c - J_2}$ where J_2^c is the critical value of J_2. This means that the boundary becomes vertical in J_2 vs T at the lowest transition temperatures. A sharp magnetic ordering transition at 23 mK (less than 0.5% of the bandwidth) would suggest a system so finely tuned to the boundary that it is much easier to believe that the system lies within an extended gap phase.

Although the evidence points towards the susceptibility feature arising from a gap in the magnetic spectrum, an alternative explanation is nuclear-dipole ordering. We consider this unlikely because (i) only 30% of Yb nuclei are magnetic,

which is below the percolation threshold (50%) for the triangular lattice, and (ii) 23 mK is quite high for nuclear dipole ordering, which is typically less than 1 mK [37]. That said, there is a noticeable nuclear Schottky anomaly in the heat capacity data in Fig. 3, which indicates some splitting the energy levels of nuclear moments. However, this does not necessarily indicate static dipolar order: the ^{173}Yb isotope (16% natural abundance) has a nonzero electric quadrupolar moment [38] whose energy levels will be split by an ionic electric field gradient at the Yb site, producing a Schottky feature without static electronic magnetism. (Furthermore, if the ordering temperature is 23 mK, a Schottky anomaly onset at 80 mK as in Ref. [25] would be much too high.) Therefore, the most natural explanation for this feature in susceptibility is a $(2.1 \pm 0.1)\mu$eV gap in the magnetic spectrum, which is estimated by fitting zero field data with $e^{-\Delta/T}$ (see Supplemental Fig. 9). This is too low to have been observed in the inelastic neutron experiment, which could not resolve features below 50 μeV.

According to the generalized Lieb-Schultz-Mattis theorem, the existence of a low-energy gap in the absence of a phase transition for a translationally invariant $S = 1/2$ triangular antiferromagnet implies that the ground state degeneracy must have a topological origin [39, 40]. Because these materials are known to be in close proximity to a QSL phase [30], this indicates that NaYbSe$_2$ lies within the QSL phase. This was suggested by previous refinements of the second-nearets-neighbor exchange [30], but the observation of a spin gap is far more direct evidence.

A further piece of evidence in favor of QSL physics is that the quantum critical effects seen in KYbSe$_2$ are suppressed in NaYbSe$_2$. More specifically, the neutron spectra in KYbSe$_2$ show energy temperature scaling [28] due to the proximity to the quantum critical point (QCP) between the 120° and QSL phase (see Figure 1). Quantum Fisher Information is a sensitive gauge to quantum criticality [41, 42] and the elevated value of nQFI = 3.4(2) [28] in KYbSe$_2$ indicates the influence of the QCP. In contrast nQFI = 2.3(5) for NaYbSe$_2$ (see Supplementary Material) is consistent with the material being beyond the QCP (where nQFI should be a maximum) and within the QSL phase where spectral intensity is more distributed [12, 18].

The existence of a low-energy gap allows us to rule out a gapless $\mathbb{U}_1$ Dirac QSL [6, 10, 11], but there are at least three competing theoretical options for gapped phases on the triangular lattice: (i) a resonating valence bond (gapped $\mathbb{Z}_2$) liquid, (ii) a valence bond crystal (VBC) [43, 44], or (iii) a chiral QSL [45, 46]. The data we present here is insufficient to fully resolve this debate, but the strong agreement with the Schwinger boson representation of a condensed $\mathbb{Z}_2$ liquid in KYbSe$_2$ [28] indicates that the gap is from $\mathbb{Z}_2$ topological order [15, 47]. Furthermore, the chiral QSL and valence bond crystal break discrete symmetries (time-reversal and crystalline, respectively) and hence have a finite-temperature phase transition, whereas the $\mathbb{Z}_2$ liquid does not. We do not observe the specific heat signature of either phase transition down to 100 mK, and no susceptibility signatures between 25 mK and 400 mK. Moreover, if the small gap were caused by a spin-Peierls instability of the U(1) Dirac spin liquid [44],
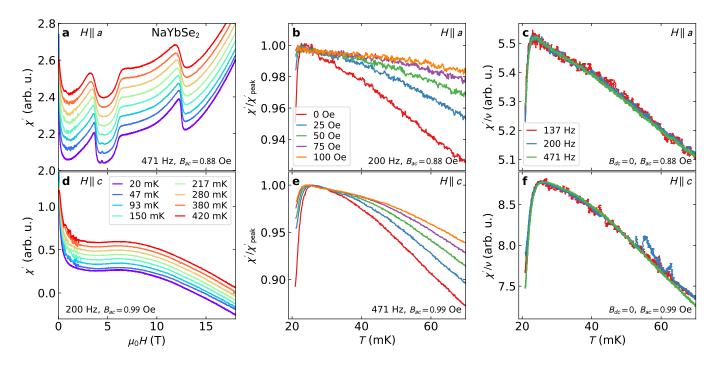
FIG. 4. Magnetic susceptibility of NaYbSe$_2$ with $B \parallel a$ (**a-c**) and $B \parallel c$ (**d-f**). The left panels (a and d) show the field-dependence, showing a 5 T drop in susceptibility from a magnetization plateau in-plane, but no plateau out-of-plane. The center panels (**b** and **e**) show the temperature dependence at low fields, with the marked drop in susceptibility at 23 mK, normalized by the peak susceptibility value. The right panels (**c** and **f**) show the frequency dependence of the drop (where susceptibility is normalized by frequency ν).

the momentum distribution of the integrated intensity over ω would be expected to closely resemble that of the U(1) Dirac spin liquid state. However, dynamical variational Monte Carlo calculations for $J_2/J_1 = 0.07$ and $J_2/J_1 = 0.09$ show that the K and M points have comparable integrated spectral weights [48], which starkly contrasts with experimental observations. Thus although we cannot uniquely identify the type of QSL with the measurements described here, the simplest interpretation of our results suggests a $\mathbb{Z}_2$ liquid, consistent with Anderson's original proposal [1].

In conclusion, we have used neutron spectroscopy, heat capacity, and magnetic susceptibility to investigate NaYbSe$_2$. The susceptibility feature either indicates a phase transition or a gap. If the former, NaYbSe$_2$ is the closest triangular delafossite material yet to a QSL; if the latter, NaYbSe$_2$ is a gapped QSL. Details of the experiment strongly suggest a gap, which means NaYbSe$_2$ lies within the 2D triangular lattice QSL phase with a (2.1 ± 0.1) μeV gap, making it stable against perturbations. Beyond susceptibility (i), further evidence for QSL physics are (ii) the coherent excitations observed in the neutron spectra are consistent with QSL simulated spectra, (iii) no static magnetic order is observed in specific heat down to 100 mK, and (iv) quantum entanglement witnesses indicates NaYbSe$_2$ has less divergent intensity than KYbSe$_2$, and is within the QSL phase. The presence of a gap allows us to rule out the gapless $\mathbb{U}_1$ and suggests a gapped $\mathbb{Z}_2$ liquid, but determining the precise nature of this ground state requires further investigation. Thus, over 50 years after Anderson's original proposal, we finally have a clean experimental realization of a triangular lattice QSL phase.

SUPPLEMENTAL MATERIALS FOR SPECTRUM AND LOW-ENERGY GAP IN TRIANGULAR QUANTUM SPIN LIQUID NaYbSe$_2$

I. SAMPLE SYNTHESIS

The samples for the neutron experiments were grown with NaCl flux and are the same as reported in Ref. [30]. A new batch of samples were grown for the susceptibility measurement. A mixture of 1.58 gram NaCl powder, 0.23 gram Yb pieces, and 0.26 gram Se pieces were sealed in a vacuumed quartz tune. The tube was vertically located in a box furnace. The temperature profile for the reaction is that the temperature was raised to 850 Celsius degree with 50 degree/hour rate, stayed 16 days, and then decreased to 750 Celsius degree with 1 degree/hour rate, and thereafter decreased to room temperature with 100 degree/hour rate. The reddish thin plates of crystals could be picked out after the whole product was washed by water.

II. NEUTRON EXPERIMENTS

We measured the inelastic spectrum of NaYbSe$_2$ using the $\sim$ 300 mg co-aligned sample used in Ref. [30] mounted in a dilution refrigerator (no magnet was used in this experiment). We measured the *hhl* inelastic scattering on the CNCS spectrometer [49] at Oak Ridge National Laboratory's Spallation Neutron Source [50], measuring at E_i = 3.32 meV, 1.55 meV, and 1.0 meV, rotating 180° to map the neutron spectrum. We measured at T = 0.1 K and 12 K for a background. The data are shown in main text Fig. 2, and were normalized to absolute units by normalizing the magnon mode measured in Ref. [30] to the nonlinear spin wave theory, such that the effective spin is 1/2.

Figure 6 shows the inelastic spectrum with an incident energy E_i = 1.0 meV, which gives an elastic line FWHM energy resolution 0.02 meV. With this resolution, no gap is observed at K.

Figure 7 shows the elastic scattering with the higher resolution E_i = 1.55 meV data. Temperature-subtraction shows no elastic scattering at hh = (1/3, 1/3), indicating an absence of long range static magnetic order. However, this may be because the CNCS spectrometer is not sensitive enough: similar CNCS scans on KYbSe$_2$ showed no static magnetism at zero-field [30], even though triple axis scans clearly showed the onset of elastic Bragg intensity [28]. Therefore, the absence of detectable NaYbSe$_2$ elastic scattering in these data does not necessarily indicate the absence of static magnetic order.

For a more complete view of the collected scattering data, Fig. 8 shows constant energy slices of NaYbSe$_2$ with E_i = 3.32 meV. Note the magnetic signal (most clearly shown in the temperature-subtracted data) has essentially no dependence on ℓ, indicating no correlations between the triangular lattice planes. Figure 9 also shows this, with plots of different integration widths along ℓ which makes no visible difference to the inelastic scattering pattern. Therefore these scattering data are very two-dimensional.

Figure 10 shows the intensity at K as a function of energy transfer. Unfortunately, because only one temperature is available, it is not possible to evaluate the presence or absence of a power-law scaling collapse to the data. Instead, we merely point out that the high energy transfer region appears to follow a power law with α = 1.74(6), consistent with the fitted KYbSe$_2$ value of α = 1.73(12) [28] (though the precise exponent depends upon the fitted energy transfer region).

III. AC CALORIMETRY

Ac calorimetry measurements under hydrostatic pressure were performed in a piston-clamp pressure cell using Daphne oil 7373 as the pressure medium using the standard steady state technique [51]. The temperature oscillations were measured using an Au/0.07%Fe-chromel thermocouple, and a constantan meander was attached to the opposite side of the sample to apply heat. The heater power was varied between 25 nW and 5 μW depending on the sample temperature. The measurement frequency was continuously adjusted to keep a constant phase relationship between the applied heat and the temperature oscillations on the thermocouple. For the lowest ($\leq$ 100 nW) powers and temperatures the frequency was fixed near 2 Hz because the signal was too small to continuously vary the frequency. Below 300 mK, it was not possible to find a frequency range where $f\Delta T_{ac}$ was constant. This indicates that the internal relaxation of the sample is likely slower than the relaxation rate to the bath. Nonetheless, the measurement would still be sensitive to phase transitions even in this temperature range.

In Fig. 11 the NaYbSe$_2$ specific heat is compared to previously published KYbSe$_2$ data [28]. The "bump" in C/T is smaller in NaYbSe$_2$ than in KYbSe$_2$, while the specific heat below 300 mK is significantly larger in NaYbSe$_2$. This indicates more of the density of states has shifted to low energies, which is consistent with the system being within a QSL phase. Note also, in main text Fig. 3 there is no significant missing entropy in NaYbSe$_2$, which again is consistent with it being in a well-defined quantum ground state rather than a glassy frozen state.

Figure 11 also shows the experimental data from NaYbSe$_2$ and KYbSe$_2$ compared to the TPQ simulations. In C/T the theoretical heat capacity maximum is at higher temperature than the experimental maximum, possibly due to a finite-size-induced gap. However, on a qualitative level the resemblance between theory and experiment is strong, and the theoretical trend is consistent with NaYbSe$_2$ having a larger second neighbor exchange J_2 than KYbSe$_2$.

IV. AC SUSCEPTIBILITY

A. Method

The ac susceptometer comprises a solenoidal coil to generate an ac magnetic field and a pair of sensing coils housed within it. The pair of sensing coils are wound in
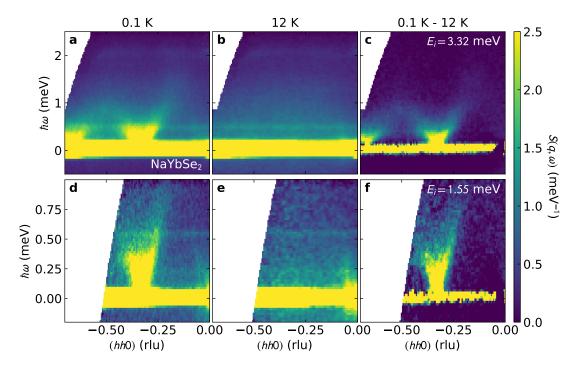
FIG. 5. Neutron scattering data on NaYbSe$_2$ in the $hh\ell$ scattering plane, integrated over ℓ < 4.5 reciprocal lattice units (rlu). The top row (a)-(c) shows scattering with E_i = 3.32 meV, the bottom row (d)-(f) shows scattering with 1.55 meV. The left column shows the raw data at 0.1 K, the middle column the background at 12 K, the right column shows the background subtracted data.
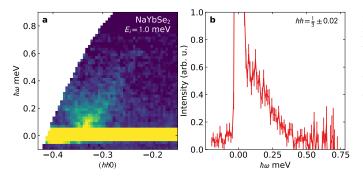

FIG. 6. NaYbSe$_2$ scattering with E_i = 1.0 meV and $|\ell| \leq 1.0$ rlu. Panel (a) shows data along hh, panel (b) shows a constant Q cut at hh = (1/3, 1/3). Intensity monotonically decreases with increasing energy, indicating a gapless spectrum to within ±0.02 meV.

opposite directions, ensuring they possess equal mutual inductance in magnitude but opposite signs. Consequently, when two sensing coils are connected in series, the induced voltage across them becomes zero. The presence of a sample positioned in the center of one of the sensing coils induces a nonzero net voltage across the coils. This induced voltage is directly proportional to the change in magnetic flux passing through the sensing coil over time. More detailed information can be found in https://nationalmaglab.org/user-facilities/dc-field/measurement-techniques/ac-magnetic-susceptibility-dc/. This setup includes a nonzero background susceptibility. Based on our experience of running this setup for over ten years, we believe that the excessive susceptibility near zero

magnetic field is due to coil background, although we did not perform a background measurement. The background in temperature scans is much smaller compared to the sample signal. Therefore, the susceptibility drop below 23 mK is due to the sample's intrinsic behavior (confirmed by the absence of such a downturn in KYbSe$_2$ data, see below). We used "Arbi. Unit" because of the background signal of the AC susceptometer.

B. Additional data

Figure 12 shows the temperature-dependent AC susceptibility at zero magnetic field up to higher temperatures than in the main text Fig. 4. Paramagnetic behavior is evident up to 500 mK, with no phase transitions visible.

Figure 13 shows susceptibility to estimate the gap of the low-temperature drop in susceptibility, which we find to be 2.1 μeV.

Figure 14 shows additional temperature-dependent NaYbSe$_2$ susceptibility data for applied fields between 1 T and 12 T. For field applied along c, there are no clear features in the data indicating phase boundaries. For field along a, there are several kinks and discontinuities. The phase diagram from temperature and field dependent susceptibility features is plotted in panel (c) of Fig. 14.

Finally, for comparison with NaYbSe$_2$, Figure 15 shows the measured in-plane susceptibility of KYbSe$_2$ (which was also measured in the same cryostat at the same time—and therefore the same temperature and field configurations—as
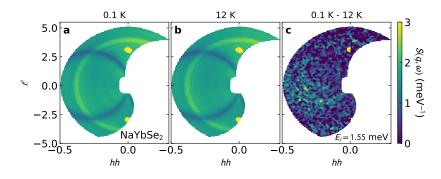
FIG. 7. NaYbSe$_2$ elastic scattering with E_i = 1.55 meV at 0.1 K (a), 12 K (b), and 0.1 K − 12 K (c), with an energy window ±0.04 meV. No static spin correlations are visible in the temperature-subtracted data, suggesting an absence of long-range magnetic order. Note that in the unsubtracted data, there are arcs of suppressed intensity from when the vertical plates of the sample holder are along the incident and scattered beams respectively, and absorption is much larger.
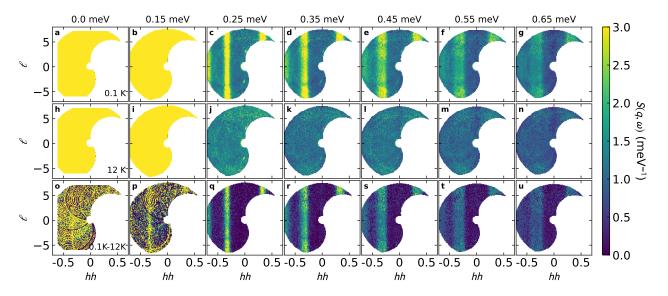

FIG. 8. Constant energy slices of NaYbSe$_2$ with E_i = 3.32 meV. The top row (a)-(g) shows the 0.1 K data, the middle row (h)-(n) shows the 12 K background, and the bottom row (o)-(u) shows the background subtracted data. Note the vertical streaks in the top and bottom row which reveals spin correlations independent of ℓ, meaning the magnetic excitations are two-dimensional and have no correlations between triangular lattice planes.

the two NaYbSe$_2$ crystals). Note the absence of a gap feature in the data, which follows a $1/T$ divergence to the lowest temperatures. Note also that the ordering transition is not visible in the data (which is admittedly somewhat noisy), again evidencing that the 23 mK downturn in NaYbSe$_2$ is not from a magnetic ordering transition.

V. THEORETICAL SIMULATIONS

A. MPS calculations

We performed MPS simulations on the J_2/J_1 model with varying values of XXZ anisotropy Δ [12, 16, 18, 53].

$$H = J_1 \sum_{\langle i,j \rangle}(S_i^x S_j^x + S_i^y S_j^y + \Delta S_i^z S_j^z) + J_2 \sum_{\langle\langle i,j \rangle\rangle}(S_i^x S_j^x + S_i^y S_j^y + \Delta S_i^z S_j^z)$$

Simulations are done on a cylinder geometry with circumference $C = 6$ and length $L = 36$ with XC boundary conditions [45] on the triangular lattice, at a maximum bond dimension of $\chi = 512$ using the *ITensor* library [54]. The ground state $|\Omega\rangle$ of the model is found using the density matrix renormalization group (DMRG). The spin-spin correlation function is determined with time evolution using the time-dependent variational principle (TDVP) with a time step of $dt = 0.1$ [18, 55–59].

$$G(\mathbf{x}, t) = \langle\Omega|\mathbf{S}_{\mathbf{x}}(t) \cdot \mathbf{S}_c(0)|\Omega\rangle$$

where the subscript c represents the central site on the cylinder. The dynamical spin spectral function is then computed as the Fourier transform of the correlation function.

$$S(\mathbf{x}, t) = \frac{1}{N} \sum_{\mathbf{x}} \int_0^\infty \frac{dt}{2\pi} e^{i(\mathbf{q}\cdot\mathbf{x} - \omega t)} G(\mathbf{x}, t)$$
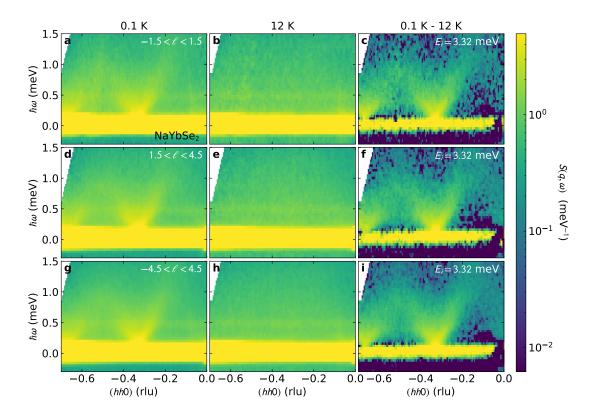
FIG. 9. NaYbSe$_2$ inelastic scattering with different windows in ℓ. The top row (a)-(c) shows ℓ centered around 0, the middle row (d)-(f) shows ℓ centered around 3, and the bottom row (g)-(i) shows ℓ integrated over both regions.
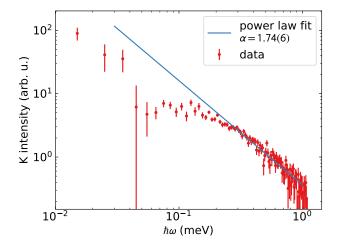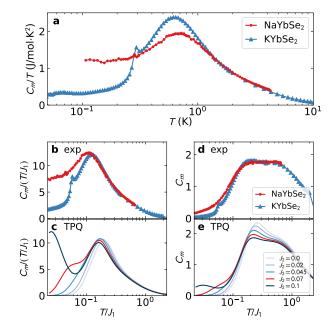

FIG. 10. Temperature-subtracted NaYbSe$_2$ neutron scattering at K. Some power law behavior appears at high energy transfers, but it seems to deviate from this at low energy transfers. The fitted exponent strongly depends upon the region fitted, but the higher energy region follows $\alpha = 1.74(6)$.

FIG. 11. NaYbSe$_2$ specific heat compared to KYbSe$_2$ (Schottky anomaly subtracted) from Ref. [28]. For NaYbSe$_2$ the nonmagnetic NaLuSe$_2$ specific heat [52] was subtracted. Panel **a** shows the specific heat, and panels **b** and **d** show the data with the temperature axis scaled by fitted J_1 [30], plotted as C and C/T respectively. Panels **c** and **e** show the TPQ calculated specific heat as a function of J_2 (in units of J_1), with the value closest to the fitted NaYbSe$_2$ shown in red.
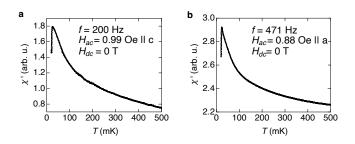
To remedy the finite time cutoff of the Fourier transform, Gaussian broadening of the time data—on the order of the cutoff $T_{\max} \sim 80$—is applied to the correlation function before transforming [18].

FIG. 12. Temperature-dependent NaYbSe$_2$ ac susceptibilities at zero dc magnetic field with the ac field along (a) the a-axis and (b) the c-axis up to 500 mK. Above 25 mK, the susceptibility shows a gradual decrease with increasing temperature, indicative of paramagnetic behavior.
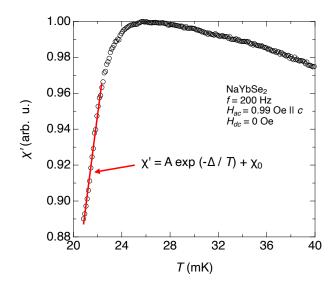

FIG. 13. AC susceptibility vs. temperature of NaYbSe$_2$ with the AC field along the a-axis. The red curve represents the fitting with $\chi' = Ae^{-\Delta/T} + \chi_0$. From this fit, we estimated the energy gap to be approximately 2.1 μeV.

B. TPQ specific heat calculations

We numerically calculated the magnetic specific heat C_m for the $S = 1/2$ AFM J_1-J_2 Hamiltonian

$$H = J_1 \sum_{\langle i,j \rangle} \mathbf{S}_i \cdot \mathbf{S}_j + J_2 \sum_{\langle\langle i,j \rangle\rangle} \mathbf{S}_i \cdot \mathbf{S}_j \qquad (1)$$

on a 27-site cluster (shown in Fig. 16) with periodic boundary conditions using the microcanonical thermal pure quantum state (TPQ) [60] method and the $\mathcal{H}\Phi$ library [61, 62], version 3.5.2. In this typicality-based approach, a thermal quantum state is iteratively constructed starting from a randomized initial vector, and associated with a temperature estimated from the internal energy. To reduce statistical errors, we averaged over 15 initial vectors. Finite-size errors are expected to mainly affect the results at low temperatures [63, 64], but not to change the trend with J_2/J_1 highlighted here.
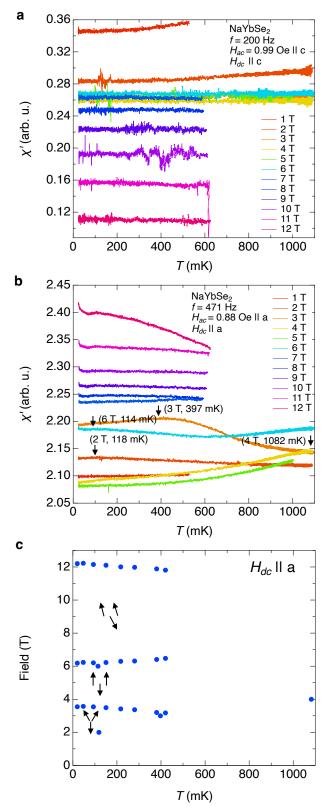

FIG. 14. (a) AC susceptibility of NaYbSe$_2$ vs. temperature at fields parallel to the c-axis from 1 T to 12 T. (b) AC susceptibility vs. temperature at fields parallel to the a-axis from 1 T to 12 T. The arrows indicate the phase transition points with respect to dc field and temperature. (c) A magnetic phase diagram of NaYbSe$_2$ field-dependent transitions with the field along the a-axis. The data points were taken from AC susceptibility measurements. The arrows represent a schematic of the spin structure for each phase.
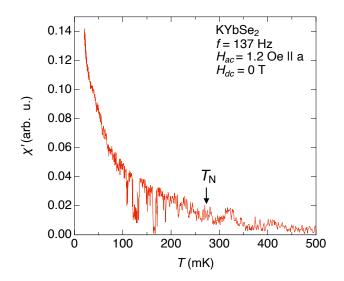
FIG. 15. AC susceptibility of KYbSe$_2$. The feature near the ordering temperature $T_N \sim 290$ mK is negligible in AC susceptibility because the magnetic moment is suppressed by strong quantum fluctuations.
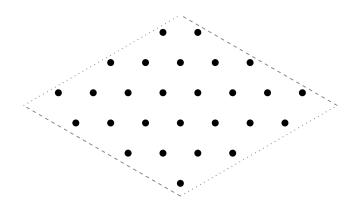

FIG. 16. Finite size cluster used for the TPQ calculations. The number of sites (27) is divisible by three to be compatible with the 120° order at low J_2/J_1. Periodic boundary conditions are applied across edges with dashed or dotted lines.

C. Phase transition through neural quantum states (NQSs)

1. NQS wave function

The NQS method utilizes an artificial neural network as a variational wave function to approximate the ground state of a target model [65]. In a system with N spin-1/2 degrees of freedom, the Hilbert space can be spanned by the S_z basis $|\sigma\rangle = |\sigma_1, ..., \sigma_N\rangle$ with $\sigma_i = \uparrow$ or $\downarrow$. Similar to image recognition tasks in which the artificial neural network converts every image input to a probability, in quantum many-body problems the NQS converts every input basis $|\sigma\rangle$ to a wave function amplitude ψ_σ. This gives the full quantum state as

$$|\Psi\rangle = \sum_\sigma \psi_\sigma |\sigma\rangle. \tag{2}$$

In this work, we employ deep residual convolutional neural networks as the variational wave function. The network contains 16 convolutional layers, each with 32 channels and 3×3 kernels, leading to 139008 real parameters in total. The GeLU activation is applied before each convolutional layer. The circular padding is utilized in the convolutional layer to realize the exact translation symmetry. The output after the last convolutional layer contains 32 channels, which is divided into two groups $x_j^{(1)}$ and $x_j^{(2)}$ each with 16 channels, and the final wave function amplitude output of the network is given by $\psi_\sigma = \sum_j \exp(x_j^{(1)} + i x_j^{(2)})$, where we sum over all elements in the 16 channels.

In addition, we apply symmetries on top of the well-trained ψ_σ to project variational states onto suitable symmetry sectors. Assuming the system permits a symmetry group represented by operators T_i with characters ω_i, the symmetrized wave function is then defined as [66, 67]

$$\psi_\sigma^{\text{symm}} = \sum_i \omega_i^{-1} \psi_{T_i \sigma}. \tag{3}$$

The applied symmetry groups in Eq. (3) are the D_6 group realizing rotation and reflection symmetries and the Z_2 group realizing the spin inversion symmetry $\sigma \rightarrow -\sigma$.

The deep network is trained by the MinSR method to approach the ground state of the triangular J_1-J_2 Hamiltonian [68]. The training employs 10000 Monte Carlo samples, 20000 steps without symmetries followed by 10000 steps with symmetries.

2. Phase transition

The transition between the 120°-ordered and the QSL phase can be detected through the spin structure factor

$$S(\mathbf{q}) = \frac{1}{N} \sum_{ij} C_{ij} e^{i\mathbf{q} \cdot (\mathbf{r}_i - \mathbf{r}_j)}, \tag{4}$$
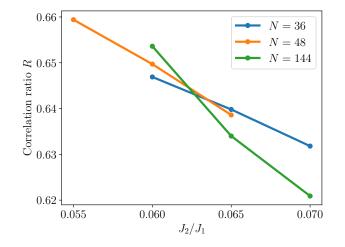

FIG. 17. Correlation ratio

where $\mathbf{q}$ denotes the momentum, and C_{ij} is the real-space spin-spin correlation given by

$$C_{ij} = \langle \mathbf{S}_i \cdot \mathbf{S}_j \rangle, \qquad (5)$$

which is obtained from the NQS wave function by Monte Carlo sampling. The 120° order is signaled by a peak in the spin structure factor $S(\mathbf{K})$ at $\mathbf{K} = (4\pi/3, 0)$. In the thermodynamic limit, $S(\mathbf{K})$ diverges only in the 120° ordered phase but not in the QSL phase.

Importantly, the numerical simulations are performed for large but finite systems, leading to finite structure factors in both phases. In order to minimize finite-size effects for the detection of phase transitions, the so-called correlation ratio R has been introduced [69–71]

$$R = 1 - \frac{S(\mathbf{K} + \delta\mathbf{q})}{S(\mathbf{K})}, \qquad (6)$$

where $\mathbf{K} + \delta\mathbf{q}$ represents the nearest neighboring momentum of $\mathbf{K}$. The correlation ratio represents a measure for the sharpness of the spin structure factor. As the system size N increases, R grows in the 120° ordered phase and decreases in

the QSL phase. Most important for the current purpose, this opposite behavior in the two phases with system sizes, generically leads to a crossing point in R for different N at the phase transition point. As shown in Fig. 17, the correlation ratio R for different system sizes indeed exhibits such a crossing at $J_2/J_1 \approx 0.063$ signaling the phase transition.

We identify two sources for uncertainties in estimating the precise quantum phase transition point, namely a variational bias and a statistical error. First, for complex quantum models such as the considered frustrated magnets we find that the variationally obtained wave function exhibits larger variational errors upon increasing system size. We observe that these errors usually have the tendency to lead to a stronger spin order and consequently to a larger correlation ratio R consistent with other works [72]. Therefore, our estimate for the phase transition point $J_2/J_1 = 0.063$ exhibits a bias towards larger values of J_2/J_1 so that we interpret 0.063 as an upper bound. Second, the measurement of R is based on an underlying Monte Carlo sampling scheme, which introduces statistical errors and leads to an uncertainty 0.001 in the critical J_2/J_1 value. In summary, the result provided in Fig. 17 lead to a bound of the critical point of the form $J_2/J_1 \lesssim 0.063 \pm 0.001$.

[1] P. Anderson, Resonating valence bonds: A new kind of insulator?, Materials Research Bulletin 8, 153 (1973).

[2] L. Savary and L. Balents, Quantum spin liquids: a review, Reports on Progress in Physics 80, 016502 (2016).

[3] C. Broholm, R. J. Cava, S. A. Kivelson, D. G. Nocera, M. R. Norman, and T. Senthil, Quantum spin liquids, Science 367, 10.1126/science.aay0668 (2020).

[4] Z. Zhu and S. R. White, Spin liquid phase of the $s = \frac{1}{2}$ $J_1 - J_2$ heisenberg model on the triangular lattice, Phys. Rev. B 92, 041105 (2015).

[5] W.-J. Hu, S.-S. Gong, W. Zhu, and D. N. Sheng, Competing spin-liquid states in the spin-$\frac{1}{2}$ heisenberg model on the triangular lattice, Phys. Rev. B 92, 140403 (2015).

[6] Y. Iqbal, W.-J. Hu, R. Thomale, D. Poilblanc, and F. Becca, Spin liquid nature in the heisenberg $J_1 - J_2$ triangular antiferromagnet, Phys. Rev. B 93, 144411 (2016).

[7] S. N. Saadatmand and I. P. McCulloch, Symmetry fractionalization in the topological phase of the spin-$\frac{1}{2}$ J_1-J_2 triangular heisenberg model, Phys. Rev. B 94, 121111 (2016).

[8] A. Wietek and A. M. Läuchli, Chiral spin liquid and quantum criticality in extended $s = \frac{1}{2}$ heisenberg models on the triangular lattice, Phys. Rev. B 95, 035141 (2017).

[9] S.-S. Gong, W. Zhu, J.-X. Zhu, D. N. Sheng, and K. Yang, Global phase diagram and quantum spin liquids in a spin-$\frac{1}{2}$ triangular antiferromagnet, Phys. Rev. B 96, 075116 (2017).

[10] S. Hu, W. Zhu, S. Eggert, and Y.-C. He, Dirac spin liquid on the spin-1/2 triangular heisenberg antiferromagnet, Phys. Rev. Lett. 123, 207203 (2019).

[11] R. Kaneko, S. Morita, and M. Imada, Gapless spin-liquid phase in an extended spin 1/2 triangular heisenberg model, Journal of the Physical Society of Japan 83, 093707 (2014).

[12] M. Drescher, L. Vanderstraeten, R. Moessner, and F. Pollmann, Dynamical signatures of symmetry-broken and liquid phases in an $s = 1/2$ Heisenberg antiferromagnet on the triangular lattice, Physical Review B 108, L220401 (2023), publisher: American

Physical Society.

[13] A. Wietek, S. Capponi, and A. M. Läuchli, Quantum electrodynamics in 2 + 1 dimensions as the organizing principle of a triangular lattice antiferromagnet, Phys. Rev. X 14, 021010 (2024).

[14] U. F. Seifert, J. Willsher, M. Drescher, F. Pollmann, and J. Knolle, Spin-peierls instability of the u (1) dirac spin liquid, arXiv preprint arXiv:2307.12295 (2023).

[15] S. Sachdev, Kagomé- and triangular-lattice heisenberg antiferromagnets: Ordering from quantum fluctuations and quantum-disordered ground states with unconfined bosonic spinons, Phys. Rev. B 45, 12377 (1992).

[16] Y.-F. Jiang and H.-C. Jiang, Nature of quantum spin liquids of the $s = \frac{1}{2}$ heisenberg antiferromagnet on the triangular lattice: A parallel dmrg study, Phys. Rev. B 107, L140411 (2023).

[17] T. Cookmeyer, J. Motruk, and J. E. Moore, Four-spin terms and the origin of the chiral spin liquid in mott insulators on the triangular lattice, Phys. Rev. Lett. 127, 087201 (2021).

[18] N. E. Sherman, M. Dupont, and J. E. Moore, Spectral function of the $J_1 - J_2$ heisenberg model on the triangular lattice, Phys. Rev. B 107, 165146 (2023).

[19] J. Ma, Y. Kamiya, T. Hong, H. B. Cao, G. Ehlers, W. Tian, C. D. Batista, Z. L. Dun, H. D. Zhou, and M. Matsuda, Static and dynamical properties of the spin-1/2 equilateral triangular-lattice antiferromagnet ba3cosb2o9, Phys. Rev. Lett. 116, 087201 (2016).

[20] S. Ito, N. Kurita, H. Tanaka, S. Ohira-Kawamura, K. Nakajima, S. Itoh, K. Kuwahara, and K. Kakurai, Structure of the magnetic excitations in the spin-1/2 triangular-lattice heisenberg antiferromagnet ba3cosb2o9, Nature Communications 8, 235 (2017).

[21] D. Macdougal, S. Williams, D. Prabhakaran, R. I. Bewley, D. J. Voneshen, and R. Coldea, Avoided quasiparticle decay and enhanced excitation continuum in the spin-$\frac{1}{2}$ near-heisenberg triangular antiferromagnet ba3cosb2o9, Phys. Rev. B 102, 064421 (2020).

[22] E. A. Ghioldi, M. G. Gonzalez, S.-S. Zhang, Y. Kamiya, L. O. Manuel, A. E. Trumper, and C. D. Batista, Dynamical structure factor of the triangular antiferromagnet: Schwinger boson theory beyond mean field, Phys. Rev. B **98**, 184403 (2018).

[23] E. A. Ghioldi, S.-S. Zhang, Y. Kamiya, L. O. Manuel, A. E. Trumper, and C. D. Batista, Evidence of two-spinon bound states in the magnetic spectrum of ba$_3$cosb$_2$o$_9$, Phys. Rev. B **106**, 064418 (2022).

[24] K. M. Ranjith, D. Dmytriieva, S. Khim, J. Sichelschmidt, S. Luther, D. Ehlers, H. Yasuoka, J. Wosnitza, A. A. Tsirlin, H. Kühne, and M. Baenitz, Field-induced instability of the quantum spin liquid ground state in the $J_{eff} = \frac{1}{2}$ triangular-lattice compound NaYbO$_2$, Phys. Rev. B **99**, 180401 (2019).

[25] K. M. Ranjith, S. Luther, T. Reimann, B. Schmidt, P. Schlender, J. Sichelschmidt, H. Yasuoka, A. M. Strydom, Y. Skourski, J. Wosnitza, H. Kühne, T. Doert, and M. Baenitz, Anisotropic field-induced ordering in the triangular-lattice quantum spin liquid NaYbSe$_2$, Phys. Rev. B **100**, 224417 (2019).

[26] Z. Zhang, X. Ma, J. Li, G. Wang, D. T. Adroja, T. P. Perring, W. Liu, F. Jin, J. Ji, Y. Wang, Y. Kamiya, X. Wang, J. Ma, and Q. Zhang, Crystalline electric field excitations in the quantum spin liquid candidate NaYbSe$_2$, Phys. Rev. B **103**, 035144 (2021).

[27] P.-L. Dai, G. Zhang, Y. Xie, C. Duan, Y. Gao, Z. Zhu, E. Feng, Z. Tao, C.-L. Huang, H. Cao, A. Podlesnyak, G. E. Granroth, M. S. Everett, J. C. Neuefeind, D. Voneshen, S. Wang, G. Tan, E. Morosan, X. Wang, H.-Q. Lin, L. Shu, G. Chen, Y. Guo, X. Lu, and P. Dai, Spinon fermi surface spin liquid in a triangular lattice antiferromagnet NaYbSe$_2$, Phys. Rev. X **11**, 021044 (2021).

[28] A. O. Scheie, E. A. Ghioldi, J. Xing, J. A. M. Paddison, N. E. Sherman, M. Dupont, L. D. Sanjeewa, S. Lee, A. J. Woods, D. Abernathy, D. M. Pajerowski, T. J. Williams, S.-S. Zhang, L. O. Manuel, A. E. Trumper, C. D. Pemmaraju, A. S. Sefat, D. S. Parker, T. P. Devereaux, R. Movshovich, J. E. Moore, C. D. Batista, and D. A. Tennant, Proximate spin liquid and fractionalization in the triangular antiferromagnet KYbSe$_2$, Nature Physics **20**, 74 (2024).

[29] T. Xie, A. A. Eberharter, J. Xing, S. Nishimoto, M. Brando, P. Khanenko, J. Sichelschmidt, A. A. Turrini, D. G. Mazzone, P. G. Naumov, L. D. Sanjeewa, N. Harrison, A. S. Sefat, B. Normand, A. M. Läuchli, A. Podlesnyak, and S. E. Nikitin, Complete field-induced spectral response of the spin-1/2 triangular-lattice antiferromagnet csybse2, npj Quantum Materials **8**, 48 (2023).

[30] A. O. Scheie, Y. Kamiya, H. Zhang, S. Lee, A. J. Woods, M. O. Ajeesh, M. G. Gonzalez, B. Bernu, J. W. Villanova, J. Xing, Q. Huang, Q. Zhang, J. Ma, E. S. Choi, D. M. Pajerowski, H. Zhou, A. S. Sefat, S. Okamoto, T. Berlijn, L. Messio, R. Movshovich, C. D. Batista, and D. A. Tennant, Nonlinear magnons and exchange hamiltonians of the delafossite proximate quantum spin liquid candidates KYbSe$_2$ and NaYbSe$_2$, Phys. Rev. B **109**, 014425 (2024).

[31] J. A. M. Paddison, M. Daum, Z. Dun, G. Ehlers, Y. Liu, M. Stone, H. Zhou, and M. Mourigal, Continuous excitations of the triangular-lattice quantum spin liquid YbMgGaO$_4$, Nature Physics **13**, 117 (2017).

[32] K. A. Ross, L. Savary, B. D. Gaulin, and L. Balents, Quantum excitations in quantum spin ice, Phys. Rev. X **1**, 021002 (2011).

[33] Z. Zhang, J. Li, W. Liu, Z. Zhang, J. Ji, F. Jin, R. Chen, J. Wang, X. Wang, J. Ma, and Q. Zhang, Effective magnetic hamiltonian at finite temperatures for rare-earth chalcogenides, Phys. Rev. B **103**, 184419 (2021).

[34] A. V. Chubukov and D. I. Golosov, Quantum theory of an antiferromagnet on a triangular lattice in a magnetic field, Journal of Physics: Condensed Matter **3**, 69 (1991).

[35] D. Sellmann, X.-F. Zhang, and S. Eggert, Phase diagram of the antiferromagnetic xxz model on the triangular lattice, Phys. Rev. B **91**, 081104 (2015).

[36] G. Quirion, M. Lapointe-Major, M. Poirier, J. A. Quilliam, Z. L. Dun, and H. D. Zhou, Magnetic phase diagram of ba$_3$cosb$_2$o$_9$ as determined by ultrasound velocity measurements, Phys. Rev. B **92**, 014414 (2015).

[37] M. Goldman, Nuclear dipolar magnetic ordering, Physics Reports **32**, 1 (1977).

[38] N. Stone, Table of nuclear electric quadrupole moments, Atomic Data and Nuclear Data Tables **111-112**, 1 (2016).

[39] M. Oshikawa, Commensurability, excitation gap, and topology in quantum many-particle systems on a periodic lattice, Phys. Rev. Lett. **84**, 1535 (2000).

[40] M. B. Hastings, Lieb-schultz-mattis in higher dimensions, Phys. Rev. B **69**, 104431 (2004).

[41] P. Hauke, M. Heyl, L. Tagliacozzo, and P. Zoller, Measuring multipartite entanglement through dynamic susceptibilities, Nat. Phys. **12**, 778 (2016).

[42] P. Laurell, A. Scheie, E. Dagotto, and D. A. Tennant, Witnessing entanglement and quantum correlations in condensed matter: A review (2024), arXiv:2405.10899 [quant-ph].

[43] B. Miksch, A. Pustogow, M. J. Rahim, A. A. Bardin, K. Kanoda, J. A. Schlueter, R. Hübner, M. Scheffler, and M. Dressel, Gapped magnetic ground state in quantum spin liquid candidate κ-(bedt-ttf)$_2$cu$_2$(cn)$_3$, Science **372**, 276 (2021), https://www.science.org/doi/pdf/10.1126/science.abc6363.

[44] U. F. P. Seifert, J. Willsher, M. Drescher, F. Pollmann, and J. Knolle, Spin-peierls instability of the u(1) dirac spin liquid (2023), arXiv:2307.12295 [cond-mat.str-el].

[45] A. Szasz, J. Motruk, M. P. Zaletel, and J. E. Moore, Chiral Spin Liquid Phase of the Triangular Lattice Hubbard Model: A Density Matrix Renormalization Group Study, Physical Review X **10**, 021042 (2020), publisher: American Physical Society.

[46] B.-B. Chen, Z. Chen, S.-S. Gong, D. N. Sheng, W. Li, and A. Weichselbaum, Quantum spin liquid with emergent chiral order in the triangular-lattice hubbard model, Phys. Rev. B **106**, 094420 (2022).

[47] F. Wang and A. Vishwanath, Spin-liquid states on the triangular and kagomé lattices: A projective-symmetry-group analysis of schwinger boson states, Phys. Rev. B **74**, 174423 (2006).

[48] F. Ferrari and F. Becca, Dynamical structure factor of the $J_1 - J_2$ heisenberg model on the triangular lattice: Magnons, spinons, and gauge fields, Phys. Rev. X **9**, 031026 (2019).

[49] G. Ehlers, A. A. Podlesnyak, J. L. Niedziela, E. B. Iverson, and P. E. Sokol, The new cold neutron chopper spectrometer at the spallation neutron source: Design and performance, Review of Scientific Instruments **82**, 085108 (2011).

[50] T. E. Mason, D. Abernathy, I. Anderson, J. Ankner, T. Egami, G. Ehlers, A. Ekkebus, G. Granroth, M. Hagen, K. Herwig, J. Hodges, C. Hoffmann, C. Horak, L. Horton, F. Klose, J. Larese, A. Mesecar, D. Myles, J. Neuefeind, M. Ohl, C. Tulk, X.-L. Wang, and J. Zhao, The spallation neutron source in oak ridge: A powerful tool for materials research, Physica B: Condensed Matter **385**, 955 (2006).

[51] P. F. Sullivan and G. Seidel, Steady-state, ac-temperature calorimetry, Phys. Rev. **173**, 679 (1968).

[52] J. Xing, L. D. Sanjeewa, J. Kim, W. R. Meier, A. F. May, Q. Zheng, R. Custelcean, G. R. Stewart, and A. S. Sefat, Synthesis, magnetization, and heat capacity of triangular lattice materials naerse$_2$ and kerse$_2$, Phys. Rev. Mater. **3**, 114413 (2019).

[53] U. Schollwöck, The density-matrix renormalization group in the age of matrix product states, Annals of Physics **326**, 96 (2011).

[54] M. Fishman, S. White, and E. Stoudenmire, The ITensor Software Library for Tensor Network Calculations, SciPost Physics Codebases , 4 (2022).

[55] J. Haegeman, J. I. Cirac, T. J. Osborne, I. Pižorn, H. Verschelde, and F. Verstraete, Time-Dependent Variational Principle for Quantum Lattices, Physical Review Letters **107**, 070601 (2011), publisher: American Physical Society.

[56] J. Haegeman, T. J. Osborne, and F. Verstraete, Post-matrix product state methods: To tangent space and beyond, Physical Review B **88**, 075133 (2013), publisher: American Physical Society.

[57] J. Haegeman, C. Lubich, I. Oseledets, B. Vandereycken, and F. Verstraete, Unifying time evolution and optimization with matrix product states, Physical Review B **94**, 165116 (2016), publisher: American Physical Society.

[58] L. Vanderstraeten, J. Haegeman, and F. Verstraete, Tangent-space methods for uniform matrix product states, SciPost Physics Lecture Notes , 007 (2019).

[59] M. Yang and S. R. White, Time-dependent variational principle with ancillary Krylov subspace, Physical Review B **102**, 094315 (2020), publisher: American Physical Society.

[60] S. Sugiura and A. Shimizu, Thermal pure quantum states at finite temperature, Phys. Rev. Lett. **108**, 240401 (2012).

[61] M. Kawamura, K. Yoshimi, T. Misawa, Y. Yamaji, S. Todo, and N. Kawashima, Quantum lattice model solver $\mathcal{H}\phi$, Comp. Phys. Commun. **217**, 180 (2017).

[62] K. Ido, M. Kawamura, Y. Motoyama, K. Yoshimi, Y. Yamaji, S. Todo, N. Kawashima, and T. Misawa, Update of $\mathcal{H}\phi$: Newly added functions and methods in versions 2 and 3, Comp. Phys. Commun. **298**, 109093 (2024).

[63] P. Prelovšek and J. Kokalj, Finite-temperature properties of the extended Heisenberg model on a triangular lattice, Phys. Rev. B **98**, 035107 (2018).

[64] J. Schnack, J. Richter, and R. Steinigeweg, Accuracy of the finite-temperature Lanczos method compared to simple typicality-based estimates, Phys. Rev. Research **2**, 013186 (2020).

[65] G. Carleo and M. Troyer, Solving the quantum many-body problem with artificial neural networks, Science **355**, 602 (2017).

[66] Y. Nomura, Helping restricted boltzmann machines with quantum-state representation by restoring symmetry, Journal of Physics: Condensed Matter **33**, 174003 (2021).

[67] M. Reh, M. Schmitt, and M. Gärttner, Optimizing design choices for neural quantum states, Phys. Rev. B **107**, 195115 (2023).

[68] A. Chen and M. Heyl, Efficient optimization of deep neural quantum states toward machine precision (2023), arXiv:2302.01941 [cond-mat.dis-nn].

[69] R. K. Kaul, Spin nematics, valence-bond solids, and spin liquids in SO(n) quantum spin models on the triangular lattice, Phys. Rev. Lett. **115**, 157202 (2015).

[70] S. Pujari, T. C. Lang, G. Murthy, and R. K. Kaul, Interaction-induced dirac fermions from quadratic band touching in bilayer graphene, Phys. Rev. Lett. **117**, 086404 (2016).

[71] Y. Nomura and M. Imada, Dirac-type nodal spin liquid revealed by refined quantum many-body solver using neural-network wave function, correlation ratio, and level spectroscopy, Phys. Rev. X **11**, 031034 (2021).

[72] L. L. Viteritti, R. Rende, A. Parola, S. Goldt, and F. Becca, Transformer wave function for the shastry-sutherland model: emergence of a spin-liquid phase (2024), arXiv:2311.16889 [cond-mat.str-el].